

Cite this: *Chem. Sci.*, 2025, 16, 20073 All publication charges for this article have been paid for by the Royal Society of Chemistry

Thermally driven conformational tuning of pyridine bis-salicylaldimine for efficient CO₂ activation and cyclic carbonate formation under mild conditions

Veenu Mishra,^{ab} Siddhi Kediya,^{ab} Devender Goud,^{ab} Diku Raj Deka,^{ab} Subhajit Chakraborty^{ab} and Sebastian C. Peter^{ib}*^{ab}

This study explores the catalytic enhancement of cyclic carbonate synthesis from CO₂ and epoxides by leveraging the conformational dynamics of pyridine bis-salicylaldimine Schiff base catalysts. These multifunctional homogeneous catalysts incorporate phenolic hydrogen bond donors, pyridine nitrogen, and imine moieties, which synergistically drive the efficient cycloaddition of epoxides with CO₂ under mild conditions and atmospheric pressure. The catalytic mechanism is governed by the conformational flexibility of salicylaldimine arms attached to the pyridine ring. Thermally induced rotation of the phenolic OH disrupts molecular planarity and weakens intramolecular hydrogen bonding, facilitating a reactive geometry that enhances catalytic performance. Fine-tuning hydrogen bond distances between the phenolic –OH and imine nitrogen emerges as a key factor influencing activity. The binary catalytic system, combining rotated pyridine bis-salicylaldimine with tetrabutylammonium iodide (TBAI), achieves exceptional efficiency, enabling cyclic carbonate formation with 82–99% conversion and 99% selectivity using only a 0.9 mol% catalyst at 80 °C and 1 bar CO₂. The system's recyclability highlights its potential for sustainable CO₂ fixation. Mechanistic insights from temperature-dependent NMR, photoluminescence studies, isotopic labelling experiments, *in situ* IR, HRMS and DFT calculations reveal molecular rotation effects, the role of pyridine nitrogen in CO₂ activation, and optimized pathways for cyclic carbonate synthesis, offering a foundation for improved catalyst design.

Received 4th April 2025

Accepted 22nd September 2025

DOI: 10.1039/d5sc02533h

rsc.li/chemical-science

Introduction

The rapid increase in atmospheric CO₂ due to industrialization, especially from the excessive burning of fossil fuels, has significantly contributed to the greenhouse effect. This has led to severe environmental consequences, including more frequent droughts and flooding globally. A potential solution to mitigate these effects involves capturing and utilizing CO₂ from the atmosphere to produce valuable chemicals, offering both environmental and economic benefits.¹ Due to great potential of CO₂ as a nontoxic, ubiquitous, and sustainable resource, CO₂ fixation and its conversion techniques may play a vital role in recycling atmospheric CO₂ into useful chemicals.^{2,3} Cyclic carbonates fall under the important class of value-added chemicals which can be utilized as green solvents,^{4–6} raw materials for polymers,^{7–10} intermediates for the synthesis of fine chemicals,^{11,12} and electrolytes in lithium ion batteries.^{13,14} In principle, the reaction between epoxides and CO₂ is a highly

exothermic reaction, thereby offering a protocol for net CO₂ emission reduction. However, this reaction cannot take place spontaneously, and suitable catalysts are generally required for the efficient conversion of CO₂. Organocatalyzed cycloadditions between CO₂ and epoxides represent an attractive approach to cyclic carbonates, because organocatalysts are usually inexpensive, readily available, and free of metal contaminants.^{15–18} The chemical community is increasingly seeking cost-effective, atom-efficient, and environmentally friendly catalytic methods that use affordable organocatalysts. Various ranges of catalytic systems including metal-mediated metal–organic frameworks (MOFs), polymers,^{8,19–26} metalosalen complexes,^{27–33} and organocatalytic systems,^{34–39} including *N*-heterocyclic carbenes (NHCs),³⁸ nitrogen-based nucleophiles,⁴⁰ ionic liquids,^{41–43} modified molecular sieves⁴⁴ *etc.*, have been utilized to catalyze the chemical fixation of CO₂ to epoxides. From the green chemistry point of view, several organic compounds or organic ligands may prove to be a good alternatives for metal mediated catalytic systems. To date, many organocatalytic systems based on pyridinium,⁴⁵ imidazolium,^{46–50} ammonium,^{51–54} and phosphonium salts^{55–59} and phenols^{60–64} have been developed as both single catalysts and co-catalysts. However, the previously mentioned catalysts often require relatively harsh conditions (high temperature and pressure) compared to metal-mediated

^aNew Chemistry Unit, Jawaharlal Nehru Centre for Advanced Scientific Research, Jakkur, Bangalore-560064, India. E-mail: sebastiancp@jncasr.ac.in; sebastiancp@gmail.com; Tel: +91 080-22082998

^bSchool of Advanced Materials, Jawaharlal Nehru Centre for Advanced Scientific Research, Jakkur, Bangalore-560064, India



catalysts and are limited by low activity, high catalyst loading, and narrow substrate scope. Current efforts in this field are focused on designing organocatalysts that are easy to synthesize and can be tuned for effective catalytic activity with both terminal and internal epoxides under mild to ambient conditions.

In a previous report, D'Elia *et al.*⁶⁴ explored a binary system of ascorbic acid with TBAI (tetrabutylammonium iodide) which showed effective conversion of terminal epoxides with CO₂ to cyclic carbonates under ambient conditions. Shirakawa *et al.*⁶⁵ demonstrated that triethylamine hydroiodide is an efficient one-component catalyst for the coupling of terminal epoxides with CO₂ at 40 °C under ambient pressure. Another contribution by Kleij and co-workers demonstrated binary organocatalytic systems based on a squaramide scaffold that are highly active catalysts for the cycloaddition reaction between internal epoxides and CO₂ at 80 °C under 30 bar of CO₂.⁶⁶ In another study, an organocatalyst was developed by Dai *et al.*⁶⁷ and they demonstrated highly active one-component organocatalysts for the titled conversion at room temperature and 1 bar of CO₂ pressure for terminal epoxides and while employing a small amount of cocatalyst (TBAI), the system becomes effective for internal epoxides under mild reaction conditions.

Recent studies established that some pyridine based organocatalysts, containing hydroxyl or carboxyl groups, play an essential role in activation of highly reactive epoxide molecules *via* the hydrogen-bonding donor group (HBD).⁶⁷ More recently, Rostami *et al.* reported that commercially available 2-picolinic acid could effectively transform the cycloaddition reaction of both internal and terminal epoxides and CO₂ under neat conditions and with lower catalyst loadings⁶⁸ (Table S1). This remarkable approach offers a viable alternative to metal-based catalysis and other previously mentioned systems. Recently a range of HBDs have been investigated such as phenols,^{69–71} glycidol,⁷² silanediols,⁷³ polyalcohol⁷⁴ fluorinated alcohols,⁷⁵ squaramides,⁶⁶ boronic acids^{76,77} and ammonium,⁷⁷ Despite the examples mentioned, there are only a few studies on the use of hydrogen-bond donor (HBD) catalysis for CO₂ fixation with internal epoxides, with the notable exception of squaramide-catalyzed CO₂ fixation with internal epoxides.⁷⁸ Metal-mediated systems are well-documented in this field due to advantages like faster overall kinetics, broad substrate compatibility, and relatively mild reaction conditions. These systems efficiently convert cyclic ether substrates, including internal di- and tri-substituted epoxides, and even oxetanes, into their corresponding cyclic carbonates under mild conditions. However, the coupling of internal epoxides with CO₂ remains challenging, with only limited progress in expanding the variety of cyclic carbonate products over the years. To develop more effective catalysts for cyclic carbonate production under ambient pressure, we explored the catalytic performance of pyridine-bridged bis-salicyldimine molecules. The pyridine ring, an efficient electron-transfer structure, serves as an ideal bridge for designing multifunctional catalysts by allowing the attachment of diverse functional groups. These types of molecules have been relatively less explored, with only eight reports (based on a SciFinder search) describing their use as

photoinduced electron transfer (PET) cation sensors,^{79,80} anti-oxidants, antimicrobial agents,⁸¹ and ligands for metal complex formation,^{82–85} with their metal complexes applied in catalysis.⁸⁶

To the best of our knowledge, the pyridine-bridged bis-salicyldimine molecule has not been utilized as an organocatalyst in any field. Here, we utilized an analogue⁸⁷ of this molecule featuring multifunctional active sites capable of activating both epoxide and CO₂. We are at the forefront of utilizing this molecule as an organocatalyst for CO₂ fixation, a topic of significant contemporary relevance. These molecules proved highly efficient in co-activating both the limiting reagent (epoxide) and gaseous substrate. In this study, we present a highly active, metal- and solvent-free binary catalytic system with optimized basicity and hydrogen-bonding properties, capable of undergoing *in situ* structural reorientation under reaction conditions. During the catalytic process, rotation of the –OH group induces a change in molecular geometry, facilitating a more favourable orientation for both epoxide activation and CO₂ insertion. This conformational flexibility enhances the catalytic performance, positioning this system as a competitive alternative to metal-based catalysts.

Our theoretical investigations further reveal that the thermally induced rotation of the phenolic –OH group towards the pyridine ring represents the most favourable orientation for the cycloaddition reaction. This rotation weakens the intramolecular hydrogen bonding between the imine nitrogen and the –OH group of the salicyldimine arm, perturbing the molecule's geometry. As a result, the active sites including the pyridine, imine, and –OH groups are brought into close proximity, facilitating efficient catalytic interactions. This system, also incorporating a 3 N organonitrogen component (central pyridine ring and two salicyldimine arms), coupled with TBAI as a co-catalyst, enables the efficient conversion of both terminal and internal epoxides into cyclic carbonates with low catalyst loading. We demonstrate that the synergistic combination of phenols, imine groups, and the pyridine moiety significantly enhances the catalytic efficiency for the epoxide-to-cyclic carbonate transformation, offering a more sustainable and energy-efficient alternative to traditional high-pressure, high-temperature systems using salophen-based catalysts.⁸⁸

Results and discussion

We studied the catalytic activity and gained its mechanistic insight into a multifunctional moiety which incorporates several active sites, such as pyridine, imine, and phenol groups. This moiety, represented here as **Cat 1** (pyridine bis-salicyldimine) (Fig. 1), and its analogues **Cat 1–5** have been synthesized by using a modified methodology of previously developed procedures (SI). This type of molecule was first synthesized and characterized by Cimerman *et al.* in 1997.⁸⁹ They also reported the crystal structure and characterization of their molecule, which showed partial but not complete alignment with the properties of **Cat 1** presented here. From this perspective, **Cat 1** represents a novel molecule, and this work is the first to report a series of pyridine-bridged bis-salicyldimine-based homogeneous organocatalysts (**Cat 1** to **Cat 5**)



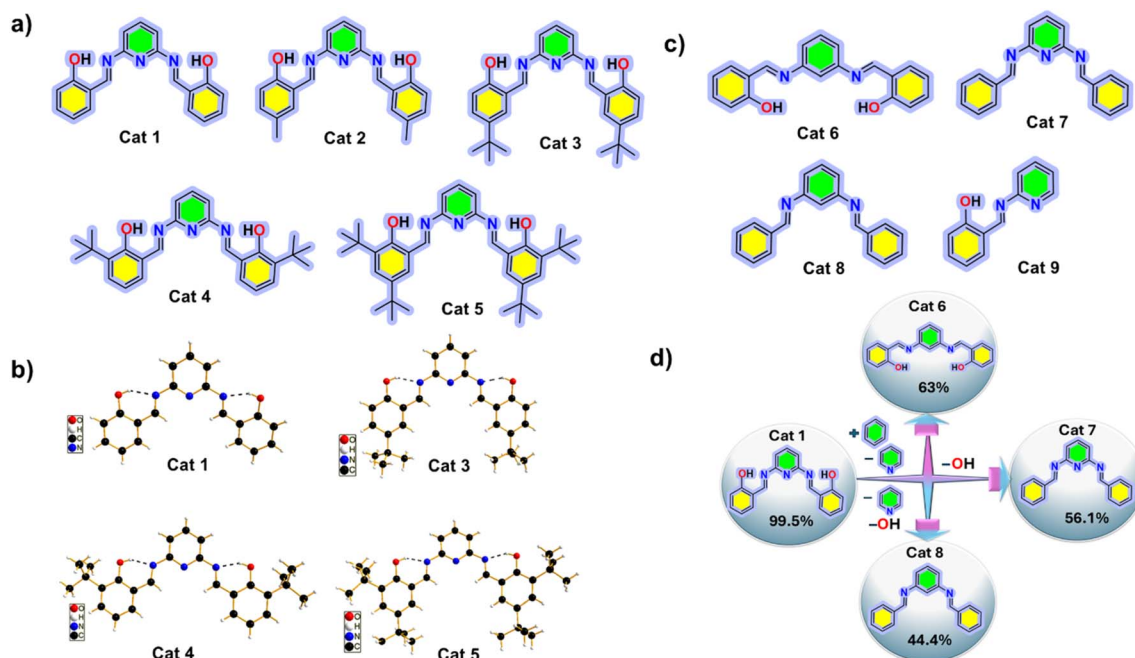


Fig. 1 (a) Schematic representation of structures of Cat 1–5 along with crystal structures of Cat 1–5. (b) The exact orientation of the molecule where OH groups of Cat 1–5 are positioned away from the pyridine N and also form H-bonding with imine N and play a role in the activation of epoxides. (c) Schematic representation of Cat 6–9 for the control study which describes the role of pyridine in catalytic performance of Cat 1. (d) Schematic representation of the role of active sites present in Cat 1.

featuring a 3 N conjugated system. Cat 1–5 have been characterized through NMR and mass spectroscopy and structures were further confirmed by the single crystal XRD technique (Fig. 1, S1–S10 and Table S2). A similar kind of 3 N conjugated system was earlier reported by Yavuz *et al.* in 2018 as a heterogeneous catalyst. It was proven to be an efficient catalyst for the synthesis of cyclic carbonate in the absence of a cocatalyst, at a pressure of 10 bar.⁹⁰

In the presented catalytic system the –OH group of the salicylaldimine arm acts as an active site for epoxide activation through H-bonding, with a lone pair of imine N atoms, which is also part of the same salicylaldimine arm.^{91,92} Another active site, the pyridine nitrogen, facilitates the rapid activation of CO₂, while the I[–] ion was used as a nucleophile to open the epoxide ring (Fig. 2). To determine the optimal conditions for the catalytic activity of the synthesized pyridine-bridged bis-salicylaldimines, we initially used styrene oxide as a model

substrate as it is considered a challenging substrate among terminal epoxides.

Several recent reports on organocatalysts have also used styrene oxide as a probe to demonstrate their activity. The reaction was carried out at 80 °C by purging with 1 bar pressure CO₂ under solvent-free and metal free conditions. Almost all synthesized pyridine-bridged salicylaldimine catalysts (Cat 1–5) exhibited moderate to good catalytic activity; however, Cat 1 demonstrated exceptional performance, likely due to its unhindered structural arrangement compared to Cat 2–5 (Fig. 1a and c). Initially, Cat 1 alone at 1 bar CO₂ and room temperature (RT) failed to yield cyclic carbonate (Fig. 3 and Table S3). Introducing TBAI as a cocatalyst transformed the system into a binary catalytic setup, yet conversion remained minimal at RT. Recognizing the need for elevated temperatures, we systematically increased it from RT to 80 °C, achieving conversions ranging from 3.5% to 99% under 1 bar CO₂. Notably, under high-pressure conditions (5 bar CO₂, 90 °C, 0.9 mol%), the catalyst exhibited 56% conversion even without a cocatalyst. The combination of Cat 1 and TBAI under neat conditions at 80 °C and 1 bar CO₂ significantly enhanced styrene oxide transformation into styrene carbonate. To clarify the specific contributions of the pyridine moiety and the –OH group to catalytic performance, we performed a systematic series of control experiments using modified catalysts. First, we investigated the role of the bridging unit by replacing the pyridine ring in Cat 1 with a benzene ring to produce Cat 6. Under otherwise identical reaction conditions, Cat 6 showed markedly reduced catalytic efficiency compared to Cat 1 emphasizing the pivotal function of the pyridine unit in catalysis (Fig. 1, 3 and

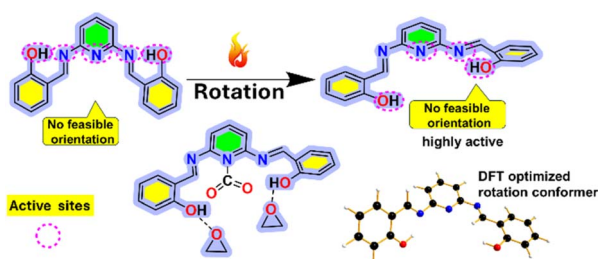


Fig. 2 Schematic representation of rotation of the –OH group and transformation of Cat 1. Active sites present in Cat 1 are shown.



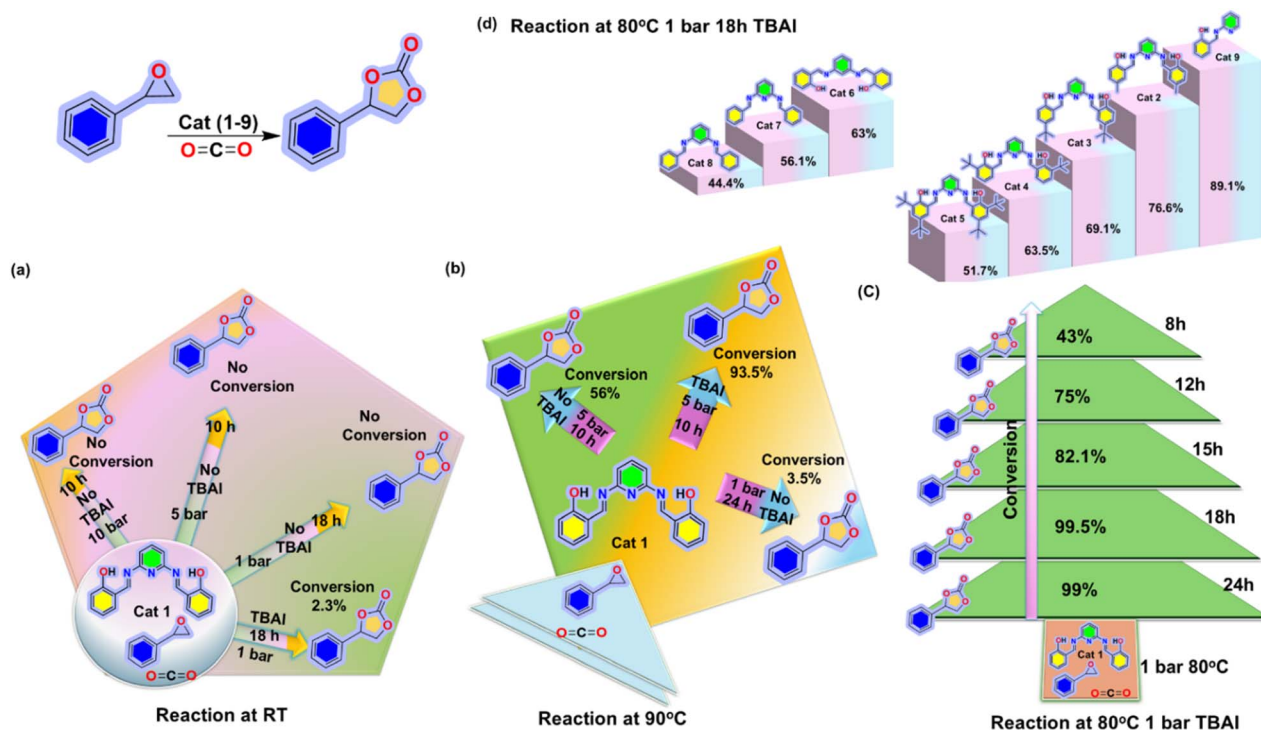


Fig. 3 (a) The catalytic activity of Cat 1 at RT with variable pressure, reaction time and cocatalyst. (b) The catalytic activity of Cat 1 at 80 °C with variable pressure, reaction time and cocatalyst. (c) Schematic showing the catalytic activity of Cat 1 at 80 °C with 1 bar variable reaction time in the presence of a cocatalyst. (d) The catalytic activity of the other catalysts (Cat 2–9) involved in controlled studies under given reaction conditions. Catalyst screening was performed for the cycloaddition of styrene oxide and CO₂ (styrene oxide (2.5 mmol), CO₂ (1 bar), and the reaction was performed neat). Conversion of styrene oxide into cyclic carbonate was assessed by ¹HNMR spectroscopy (CDCl₃) of the crude mixture. The selectivity towards cyclic carbonate was >99%, and only the *cis* isomer was formed (Table S3).

Table S3). This finding aligns with earlier reports from Hirose *et al.* and Bischoff *et al.*^{93,94} However, for the activation of pyridine, high pressure and higher loading of the catalyst/cocatalyst are required as mentioned in their report. We further explored the significance of the –OH group by synthesizing Cat 7, which lacks the –OH group, and Cat 8, which lacks both the pyridine ring and the –OH group. Comparative testing under standard conditions revealed that Cat 6, Cat 7, and Cat 8 all demonstrated significantly lower activity than Cat 1. These results indicate that both the pyridine moiety and the –OH group are crucial for optimal catalytic performance (Fig. 1d, 3 and Table S3).

Thus, the observed catalytic activity of Cat 1 could be attributed mainly to incorporation of closer proximity of the catalytic sites enabling the activation of both substrate epoxide and CO₂ simultaneously. To assess the role of the two –OH groups in Cat 1 for this conversion, we synthesized Cat 9 and evaluated its catalytic activity. Cat 9 demonstrated lower efficiency compared to Cat 1, highlighting that the presence of all three nitrogen atoms and both –OH groups is crucial for optimal catalytic performance. If we look at the theoretically optimized structure of Cat 1, two –OH groups are present in the structure, one is H-bonded with the imine N atom and the other is free (Fig. 2 rotational conformer). The H-bonded –OH group was activating the epoxide due to its fast relatively non-H-bonded OH group. When the –OH group forms a hydrogen

bond with the imine in a Schiff base, it becomes polarized, enhancing the partial positive charge on the hydrogen atom.⁹¹ This increased positive character facilitates interaction with the nucleophilic oxygen of the epoxide ring, reducing electron density on the epoxide oxygen. This polarization makes the carbon atoms of the epoxide more electrophilic and thereby more susceptible to nucleophilic attack, promoting faster ring opening and catalytic activation.⁹⁵ On the other hand, the activation of epoxide also takes place on the non-H-bonded –OH but in sluggish mode due to lack of polarization.⁹⁶ In Cat 9, activation occurs solely at the hydrogen-bonded –OH group due to the absence of non-hydrogen bonded –OH groups. As a result, Cat 9 exhibits slightly lower conversion rates compared to Cat 1, as shown in Fig. 3 and Table S3.

For further optimization and obtaining the best catalytic activity of the cycloaddition reaction of styrene oxide on the basis of structural arrangements, Cat 2–5 were subjected to further testing as they feature bulky substituents at various positions on the salicylaldehyde moiety. This investigation aimed to evaluate the influence of steric hindrance in conjunction with TBAI under consistent reaction conditions (Fig. 3 and Table S3 entry 13–16).

The cyclic carbonate was obtained in less to moderate conversion, indicating that all of them are active catalysts for promoting the reaction. Moreover, Cat 2 and Cat 3 afforded the cyclic carbonate in comparable conversion, though both were



lower than the conversion obtained by **Cat 1** due to the presence of methyl and tertiary butyl groups at the *p*-position. The presence of bulky groups at the *p*-position did not significantly hinder the rotation of the –OH group. However, **Cat 4**, which has a *tert*-butyl group at the *o*-position, likely restricts the rotation of the –OH group, resulting in a lower conversion compared to **Cat 1**, **Cat-2**, and **Cat 3**. In the case of **Cat 5**, a lower conversion was observed, likely due to the presence of bulky *tert*-butyl groups at the 3,5-positions of the salicylaldehyde arms, which effectively restricted the rotation of the –OH group. Additionally, **Cat 5** exhibited low solubility in the epoxide, and the reaction mixture remained poorly soluble even after completion. Analysis of the Cambridge crystal structure database revealed that there is only one crystal structure of pyridine bridged bis-salicylaldehyde ligands which were derived from 2,6-diaminopyridine and two aldehydes. In **Cat 1–5**, the phenols are intramolecularly bonded to the imine group but are positioned away from the pyridine ring, as illustrated in Fig. 4.

Since the crystal structures of **Cat 1** and 3–5 were not previously reported, we determined their single crystal structures to investigate the nature of the intramolecular hydrogen bonding between the phenols and the imine group. Despite numerous crystallization attempts, achieving high-quality crystals of **Cat 2** proved challenging and remained unattainable. In **Cat 1** and 3–5, the crystal structures reveal that the current orientation is not favourable for catalysis as we could not get the desired product at RT. Since catalysis occurs in the solution state, the orientation may change in solution, potentially influenced by temperature, leading to the formation of different analogues during the reaction. The crystal structure analysis of **Cat 1** and related

compounds (3–5) highlights the critical roles of steric hindrance, hydrogen bonding, and deviations from planarity in shaping their catalytic performance. Among the series, **Cat 1** is the least sterically hindered and exhibits significant deviation from planarity, with a twist angle of 9.85°, surpassed only by **Cat 5**. This perturbation in planarity is proposed to facilitate the rotation of the –OH groups upon heating. **Cat 1** forms moderate hydrogen bonds with distances of 1.861 Å (O1–H1⋯N3) and 1.886 Å (O2–H2⋯N2), indicating relatively weak interactions (Fig. 4).

These moderate bond lengths suggest a balance between stability under mild conditions and susceptibility to thermal disruption. Upon heating, the increased vibrational energy destabilizes these weak hydrogen bonds, further perturbing the molecular structure. This disruption enables the –OH groups to rotate closer to the pyridinic nitrogen, potentially altering the structural and electronic properties of the system. The observed hydrogen bond variations in **Cat 1** highlight how subtle shifts in H-bond lengths influence molecular stability, orientation, and interaction strength within catalytic sites.

One hydrogen bond is relatively weaker, making it more susceptible to thermal disruption, which allows the –OH group to rotate toward the pyridine ring at higher temperatures. This rotation is facilitated by the minimal steric hindrance due to the lack of substituents on the salicylaldehyde arm, which supports the conformational flexibility necessary for efficient catalysis.

Meanwhile, the stronger hydrogen bond, though not fully disrupted, may weaken just enough to induce rotation of the –OH group in the opposite direction, causing a polarity shift. This subtle reorientation of the –OH group enables favourable

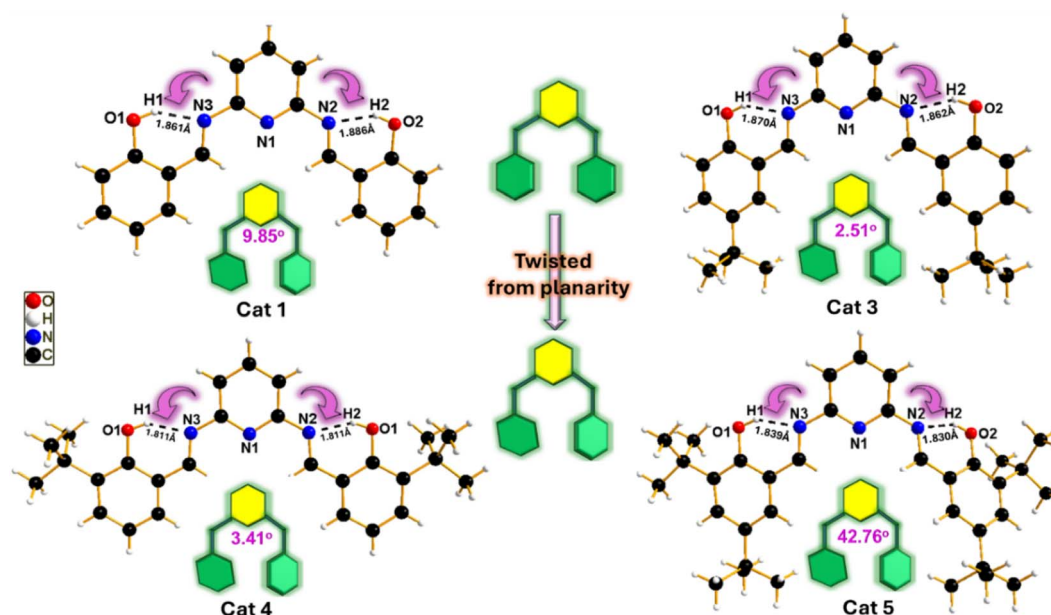


Fig. 4 The crystal structures of **Cat 1** and its analogues (3–5) revealing the presence of intramolecular hydrogen bonds between the –OH groups and imine nitrogen atoms, specifically (O1–H1⋯N3) and (O2–H2⋯N2). These structures also provide insights into deviations from planarity, quantified by measuring the angles between two defined planes within the molecules. The observed deviations from planarity are proposed to facilitate the rotation of the –OH groups, which in turn enhances the catalytic activity by influencing the structural flexibility and electronic environment of the active site.



conformational adjustments, allowing **Cat 1** to achieve higher catalytic efficiency compared to **Cat 3–5**. This idea aligns with earlier studies, such as Cimerman *et al.*,⁸⁹ which discussed the possibility of –OH group rotation under external forces, further underscoring the impact of structural flexibility⁹⁷ on catalytic performance (Fig. 4). In contrast, other catalysts of this series **Cat 3–5**, with more symmetric hydrogen bond distances and more planarity as compared to **Cat 1**, restrict –OH rotation and diminish catalytic activity due to increased steric hindrance from substituents in the *ortho* and *para* positions (Fig. 4). Specifically, in **Cat 5**, steric hindrance from *tert*-butyl groups at the 3,5-positions of both the salicylaldimine arms prevents the optimal rotation of the –OH group, even though **Cat 5** exhibits the highest nonplanarity with an angle of 42.76°.

This steric restriction and nearly symmetric bond distance (1.839 Å (O1–H1...N3) and 1.830 Å (O2–H2...N2)) prevent the molecule from achieving the ideal conformation for catalysis, which significantly limits activity. Under neat conditions, however, **Cat 5** can still catalyze conversion (using 1.8 mol% **Cat 5** and TBAI with a 1 : 1 ratio at 10 bar CO₂ at 100 °C, 24 h), achieving up to 93% conversion, though its steric limitations hamper overall efficiency. Thus, these structural and electronic insights reveal how subtle variations in hydrogen bonding and steric factors shape the catalytic effectiveness of pyridine-salicylaldimine systems (Fig. 5).

It should be noted that **Cat 1** successfully converted propylene oxide and epichlorohydrin into the corresponding cyclic carbonates at 1 bar CO₂, 80 °C, over 24 hours, without the need of a cocatalyst. This efficiency is attributed to the less hindered structure of **Cat 1** and the electron withdrawing nature of the epoxide. Additionally, **Cat 1** was able to convert other terminal epoxides into their corresponding carbonates at 5 bar

CO₂ over 10 hours, also without a cocatalyst, though the conversions were lower (Table S4).

Remarkably, these new homogeneous catalytic sites did not require high pressure, any metals or solvent to promote the reaction for the terminal epoxide but they still required high pressure and temperature for the internal epoxides to convert them into their corresponding cyclic carbonates in good yield. However, under the given reaction conditions, the transformation of cyclohexene oxide to cyclohexene carbonate has been observed up to 71% conversion. But beyond this we couldn't observe the same conversion despite using higher catalyst/cocatalyst loading under the same reaction conditions. Comparison in entries 1–7 in Table 1 reveals that a 1 : 1 ratio of **Cat 1** to TBAI is sufficient to achieve excellent conversion. Deviations from this ratio, however, may result in a loss of conversion efficiency. Our findings indicate that this level of catalyst/cocatalyst loading is lower compared to previously reported catalytic systems.^{67,68} Lowering the amount of **Cat 1** from 0.9 mol% to 0.45 mol% resulted in a substantial decrease of 68.6% in conversion. Conversely, increasing the catalyst loading to a 1 : 2 ratio resulted in a 99% conversion of styrene oxide to its

Table 1 Influence of catalyst loading on catalytic activity of **Cat 1**

Entry	Catalyst	Cocatalyst	Conv (%)
1	0.9	—	0
2	1.8	—	0
3	3.6	—	50
4	0.9	1.8	99
5	0.9	0.9	99.5
7	0.45	0.45	68.6

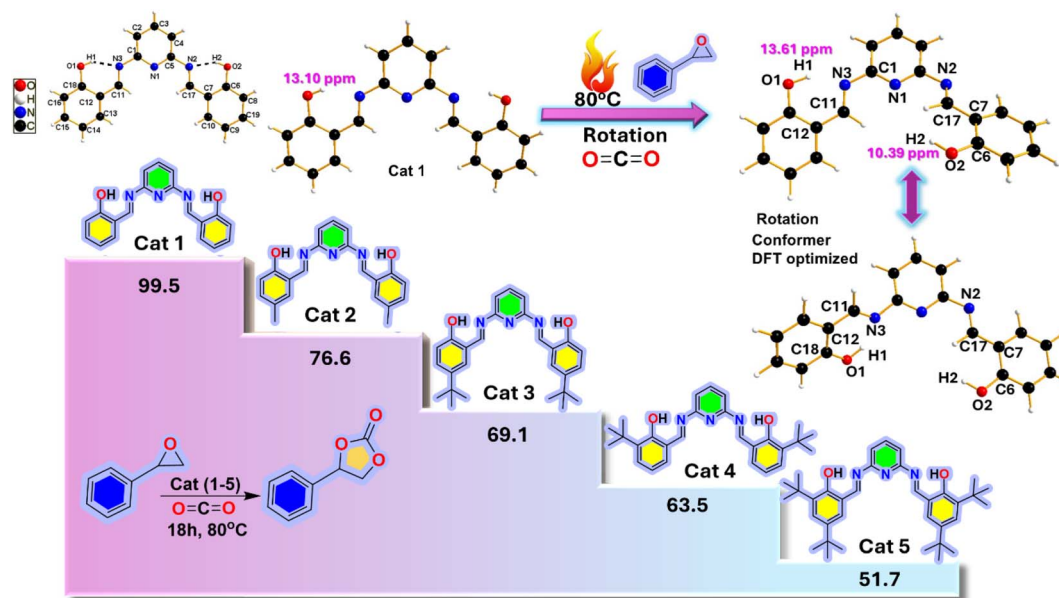


Fig. 5 Figure illustrating the descending order of catalytic activity of **Cat 1–5** for the synthesis of styrene carbonate from styrene oxide and CO₂ under the reaction conditions (1 : 1 ratio of catalyst/cocatalyst, 80 °C, 18 h, 1 bar CO₂). **Cat 1** showed the highest activity as compared to the other catalysts **Cat 2–5** due to its less hindered structural arrangement. The upper part shows the DFT optimized rotated structure of **Cat 1** obtained during the reaction under given conditions, also consistent with the NMR spectra. This orientation facilitates the catalytic performance of **Cat 1**.



corresponding carbonate. Additionally, reducing the reaction time to 15 hours yielded a conversion of 82.1%, 12 hours resulted in 75%, and 8 hours resulted in 43% conversion of the epoxide to the resultant carbonate. With optimized reaction conditions, further, we aimed to explore the generality of **Cat 1** for the coupling of CO₂ with various epoxides including aliphatic, aromatic, and ether groups under the optimized conditions.

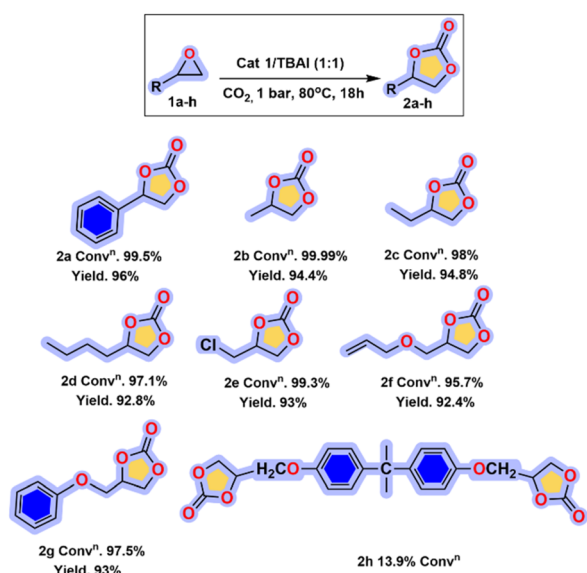
As shown in Scheme 1, all epoxides (**1a–h**) were transformed into the resultant cyclic carbonates with good to excellent quantitative yields. Alkyl substituted epoxide **1b** along with large side chain **1c** and **1d** were converted smoothly with 99.99%, 98% and 97.1% conversions. The coupling of glycidyl ether derivatives **1f** and **1g** delivered the corresponding products **2f–2g** in 95–97%. We tried to transform functionalized bisepoxide **1h** into the corresponding cyclic carbonate **2h** but due to its more steric hindrance it is restricted from entering the cage of **Cat 1** to reach the –OH group for activation, and therefore nominal conversion has been observed. To investigate the mechanism of this catalytic transformation, it's crucial to understand the orientation of the catalytic molecule.

Cat 1 was inactive at room temperature, whether used alone or in combination with TBAI. This lack of activity may be attributed to the orientation of the molecule, as indicated by its crystal structure. In the crystal structure, both –OH groups are positioned away from the pyridine N and instead form strong intramolecular hydrogen bonds with the lone pair of the imine nitrogen atom. This orientation is not conducive to the reaction because the activation sites for the epoxide and CO₂ are not in close proximity. As a result, the insertion of CO₂ into the epoxide is hindered due to this unfavourable orientation. Therefore, the reaction does not occur at room temperature

(RT), even with the addition of a cocatalyst. When the temperature is increased to 40 °C, 60 °C, and 80 °C, the reaction initiates, but the conversion at 40 °C is minimal. This low conversion at 40 °C may be because the temperature is insufficient to alter the molecular orientation. However, at 60 °C, the conversion is still not up to the mark *i.e.* 67.3%. When the temperature is raised to 80 °C, a conversion of 99.5% is achieved. This remarkable transformation is likely due to the weakening of hydrogen bonding between the –OH group and the imine nitrogen atom, which facilitates bond rotation. As a result, the –OH group moves closer to the pyridine nitrogen atom and transforms **Cat 1** into its favourable orientation for the activation of the epoxide and CO₂, leading to a more rapid insertion of CO₂.

To validate the above hypothesis, we conducted temperature-dependent NMR experiments in DMSO-d₆ to investigate the rotation of the –OH group in **Cat 1**. Initially, NMR analysis of the pristine ligand in DMSO-d₆ showed a peak at 13.10 ppm corresponding to the –OH group and a peak at 9.70 ppm for the –HC=N group (Fig. S34a and b). Upon adding the substrate styrene oxide, several new peaks appeared. The –OH peak at 13.10 ppm shifted downfield to 13.61 ppm, attributed to styrene oxide interacting with the hydrogen-bonded H atom of the phenol group.^{98,99} This interaction weakens the hydrogen bonding between the phenol –OH and the imine nitrogen, while strengthening the hydrogen bond between the epoxide oxygen and the –OH hydrogen. A new peak emerged at 10.39 ppm,¹⁰⁰ corresponding to a non-hydrogen-bonded –OH group, which can rotate and position itself near the pyridine nitrogen in **Cat 1**, as shown in Fig. 6a, b, S34a and b. Additionally, the –HC=N peak shifted from 9.70 to 9.48 ppm, indicating that **Cat 1** is oriented favourably for reaction initiation. Upon increasing the temperature from room temperature to 80 °C and conducting temperature-dependent NMR, we observed a notable upfield shift in both the hydrogen-bonded and non-hydrogen-bonded –OH peaks and the –HC=N peak. The hydrogen-bonded –OH peak showed a significant upfield shift, indicating the weakening of the hydrogen bond between the –OH group and the imine nitrogen lone pair at elevated temperatures. Conversely, the non-hydrogen-bonded –OH group exhibited only a marginal shift, suggesting slower activation of the epoxide at this site. This study is further supported by our DFT calculations which confirm the structural changes and their impact on the catalytic process (Fig. S36). As noted, the nitrogen atom in the pyridine moiety participates in CO₂ activation. To examine pyridine's role in catalysis, we performed a ¹⁵N NMR study in CDCl₃, as **Cat 1** was highly soluble in this solvent. A new ¹⁵N NMR peak appeared at 236 ppm and shifted upfield compared to the pristine compound, indicating an interaction between the pyridine N and CO₂. This interaction was confirmed by the upfield shift from 252 ppm to 236 ppm ($\Delta\delta = 16$ ppm), attributed to the engagement of the pyridine N with CO₂ as the intensity of the pyridine N peak at 252 ppm has decreased significantly (Fig. 6c).

This type of upfield shift in ¹⁵N NMR was also observed by Lai *et al.* in 2007 during the protonation of 2-aminopyridine, suggesting that the strong shielding arises from a positive



Scheme 1 Substrate scope for the addition of CO₂ to terminal epoxides. Conditions: epoxide **1** (2.5 mmol), CO₂ (1 bar), (0.9 mol%), TBAI (1.8 mol%), 80 °C, 18 h, the reaction was performed neat. Yields relate to products isolated by column purification. The selectivity towards **2a–h** was $\geq 99\%$ (Fig. S11–S25).



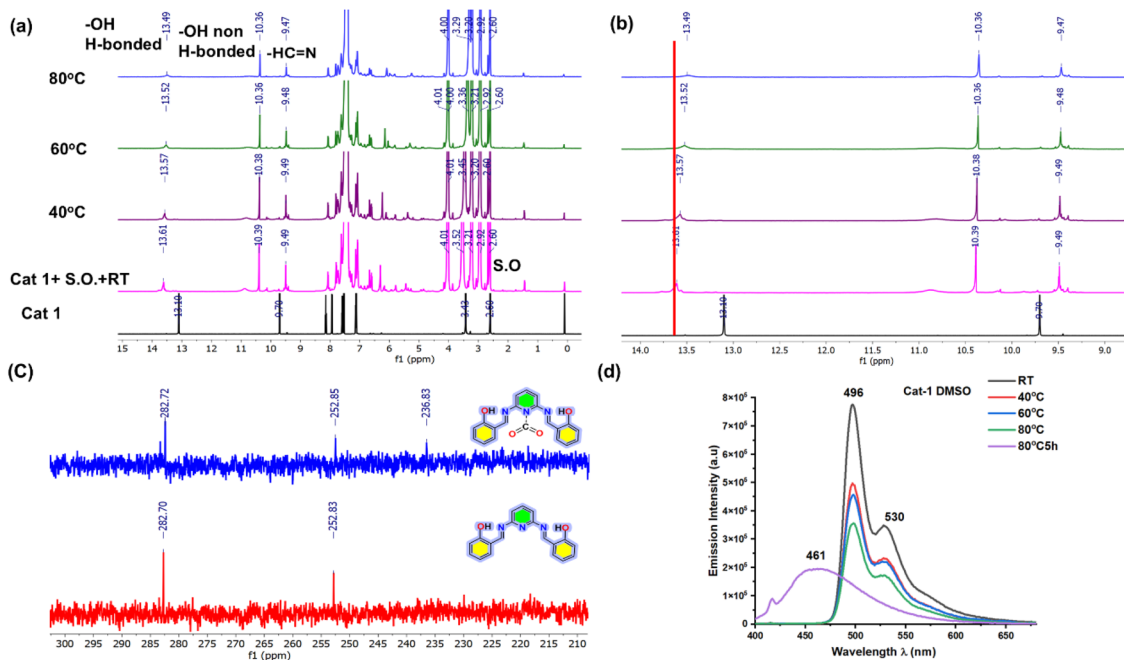


Fig. 6 (a) Temperature dependent ¹H NMR study in DMSO d₆. The ratio of Cat 1 and styrene oxide was 1 : 10 and taken at variable temperature as shown in the figure. (b) Zoomed part of 9–14 ppm chemical shift part, which clearly showed shifting on increasing temperature. (c) ¹⁵N NMR of Cat 1 and CO₂ coordinated Cat 1. In this NMR, activation of CO₂ was mainly initiated by pyridine N which generates a new peak at 236 ppm N coordinated CO₂. (d) Temperature dependent photoluminescence data of Cat 1 at different temperatures. At RT, 40 °C, 60 °C and 80 °C it showed the same pattern of the plot with decreased PL intensity. However, on further heating Cat 1 up to 5 h at 80 °C, a blue shift has been observed with a different pattern of the plot.

charge at the pyridine nitrogen.¹⁰¹ This indicates that the strong shielding observed in these molecules originates from the positive charge on the pyridine nitrogen. While this positive charge causes significant shielding, it is somewhat lower than that observed in the protonation of 2-aminopyridine. The interaction of CO₂ with the pyridine nitrogen results in reduced shielding, likely because the two oxygen atoms in CO₂ limit the nitrogen's ability to experience strong shielding, unlike the more pronounced effect seen with hydrogen interaction.

To study the thermally induced conformational rotation of Cat 1, absorption and fluorescence analysis were conducted in DMSO. The absorption spectrum of Cat 1 in DMSO displayed a maximum at 370 nm, while the fluorescence spectrum showed a primary emission peak at 496 nm, corresponding to the enol form of Cat 1 (Fig. S35).

Additionally, a minor emission feature observed at 530 nm indicates the presence of a small amount of the keto form due to excited-state intramolecular proton transfer (ESIPT).^{102,103} In DMSO, Cat 1 predominantly exists in the enol form in a singlet state that facilitates dynamic intramolecular rotations by weakening H-bonding and C=N isomerization, effectively suppressing the ESIPT process and favouring non-radiative decay from the excited state.¹⁰⁴ Temperature-dependent photoluminescence measurements revealed that the planar *cis*-enol form of Cat 1 transitions to a flipped *cis*-enol conformation upon heating. This transition is accompanied by increased rotational and vibrational freedom of the salicylaldimine arms and the C=N bond, leading to enhanced non-radiative decay pathways and reduced fluorescence intensity.¹⁰⁵ When Cat 1 is

heated in DMSO at 40 °C, 60 °C, and 80 °C, a progressive quenching of fluorescence intensity is observed, likely due to the suppression of the ESIPT process. Upon extended heating at 80 °C for up to 5 hours, a blue shift in the emission maximum to 461 nm is detected, indicating thermally induced structural changes. Notably, this structural transformation is distinctly characterized by the merging and blue shifting of the primary emission peak from 496 nm to 461 nm (Fig. 6d). This shift signifies the disruption of the intramolecular hydrogen bond between the phenolic –OH group and the imine nitrogen, driven by the formation of intermolecular hydrogen bonding between DMSO and the –OH group of the salicylaldimine arm in the flipped conformation.¹⁰⁶ Heating induces a complete rotation of the N3–C11–C12 bond and a partial rotation of the phenolic C5–N2–C17–C7 bond, collectively causing a significant weakening or disruption of the intramolecular hydrogen bonds between the phenolic –OH groups and imine N atoms on both sides. The NMR and DFT analyses are also consistent with this rotation. The extent of disruption depends on the relative strength of each hydrogen bond (as shown in Fig. 4, 5 and S36). This conformational rotation is stabilized by intermolecular hydrogen bonding between DMSO and the phenolic –OH groups of Cat 1. Under the reaction conditions used in our study, the rotation is further stabilized by styrene oxide, which acts as both a solvent and a reactant, enhancing the stability of the thermally induced conformational adjustment.

After evaluating the reactivity of Cat 1 with the combination of TBAI toward the transformation of terminal epoxides into their corresponding carbonate, we tried to extend the substrate



Table 2 Cyclohexene oxide (2.5 mmol), CO₂ (1 and 10 bar, 18 h), the reaction was performed neat. Conversion of cyclohexene oxide into cyclic carbonate was assessed by ¹HNMR spectroscopy (CDCl₃) of the crude mixture. The selectivity towards cyclic carbonate was >99%, and only the *cis* isomer was formed

Entry	Cat 1	TBAI	Temp (%)	Pressure	Conv ^a
1	0.9	0.9	80	1	22.8
2	0.9	1.8	80	1	71
3	0.9	3.6	80	1	56
4	1.8	3.6	100	10	96
5	4	0	100	10	0
7	6	6	100	10	86

scope by using internal epoxides, although internal epoxides are challenging substrates due to their high steric hindrance nature. To begin with internal epoxides, we optimized reaction conditions by employing cyclohexene oxide catalysed by **Cat 1** and TBAI. The results are presented in Table 2. Low conversions were obtained for the synthesis of cyclohexene carbonate under the given reaction conditions which were used for terminal epoxides (1 bar CO₂ 80 °C, 18 h, and 1 : 1 **Cat 1**/TBAI loading).

An increase in the **Cat-1**/TBAI ratio from 1 : 1 to 1 : 2 led to a significant enhancement in catalytic activity, achieving 71% conversion at 1 bar CO₂. However, further increasing the ratio to 1 : 4 under the same conditions did not yield any substantial improvement. This trend reflects an inverse relationship between the iodide concentration and catalytic efficiency, consistent with the literature on CO₂ epoxide coupling involving internal epoxides. At higher iodide loadings, the equilibrium likely shifts toward ring-opened intermediates and the system experiences increased ionic congestion, both of which hinder the ring-closing step and reduce overall catalytic performance.^{107,108} To overcome these limitations and improve the

yield, the reaction conditions were further optimized by increasing both the **Cat 1**/TBAI ratio to 2 : 4 and the temperature from 80 °C to 100 °C for 18 hours. Under these conditions, a dramatic enhancement in catalytic activity was observed, with **Cat 1** delivering a conversion of 96%. Moreover, in the absence of TBAI no conversion was observed at 10 bar. After selection of optimized conditions for the synthesis of cyclohexene carbonate, we emphasized the transformation of other internal epoxides into their corresponding cyclic carbonates. The results are shown in Fig. 7a. Under these optimized conditions, fused bicyclic carbonates cyclohexene and cyclopentene carbonates were obtained with excellent conversions (96% and 92.7%) and selectivity (≥99%).

Interestingly, vinyl-substituted bicyclic carbonate was obtained with 89.6% conversion and excellent selectivity. Finally, we turned our attention to the transformation of nonbicyclic epoxides *trans*-stilbene oxide: the reaction of *trans* stilbene oxide to give *trans* stilbene carbonate with 3.2% conversion. These are very challenging substrates, due to their high steric hindrance structural arrangement. Because of its structural arrangement, it may not be able to enter the cage, formed by **Cat 1** for activation. Much less product was obtained despite using higher catalyst/cocatalyst loading and a longer reaction time of 48 h. In order to check the practicality of this catalytic process, a scale-up reaction was carried out (Fig. 7b) under the optimized conditions for the terminal mono-substituted epoxide (*i.e.*, 0.9 mol%, 0.9 mol% TBAI, 80 °C, 18 h, CO₂ 1 bar, neat). Butylene oxide **1c** was transformed into the resultant cyclic carbonate **2c** in 98% conversion.

Recyclability of catalysts

Recyclability is a critical feature for the potential application of catalysts in cost-effective and environmentally sustainable

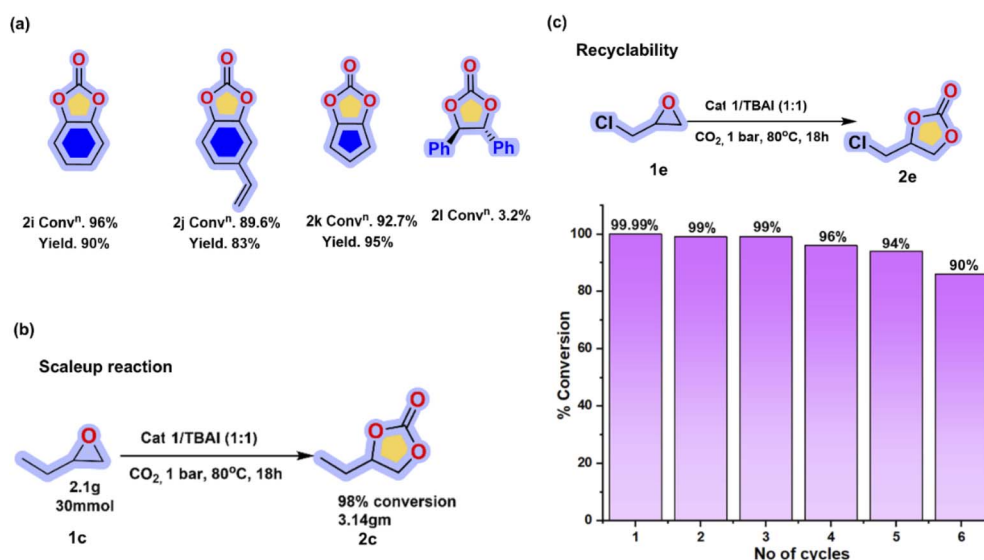


Fig. 7 (a) Substrate scope for the addition of CO₂ to internal epoxides. Conditions: epoxide **1** (2.5 mmol), CO₂ (10 bar), **Cat 1** (1.8 mol%), TBAI (3.6 mol%), 100 °C, 18 h, the reaction was performed neat. Yields relate to products isolated by column purification. The selectivity towards 2i–l was ≥99% (Fig. S26–S33). (b) Recyclability: Recycling of **Cat 1** in the coupling reaction of epichlorohydrin **1e** and CO₂ under optimized reaction conditions: catalyst amount (0.9 mol%), 1 bar CO₂, 80 °C, 18 h. (c) Scaleup: A scaleup reaction with substrate **1c**.



processes. Many recently reported homogeneous catalysts struggle with efficient recycling due to difficulties in isolation from the reaction mixture and instability under high-temperature and high-pressure conditions. In contrast, the reusability and stability of the **Cat 1**/TBAI binary system were evaluated. Due to its insolubility in diethyl ether, **Cat 1** was successfully recovered after the reaction of CO₂ with epichlorohydrin (80 °C, 1 atm CO₂, 18 h) by extraction of the cyclic carbonate and drying the catalyst under vacuum for reuse. The results demonstrated that the catalytic activity remained stable across five cycles, with only a slight reduction in activity observed during the sixth cycle, indicating the high stability of the system. Therefore, the pyridine bis-salicylaldehyde/TBAI catalytic system proves to be a highly practical and reusable catalyst for the CO₂-epoxide cycloaddition reaction, demonstrating its potential for sustainable applications in industrial processes (Fig. 7c and Table S5).

DFT studies

To validate the structural changes, DFT studies were carried out to investigate the rotation of the phenolic ring around the specified bond (details are in Note 1 in the SI and Fig. S37–S39 in SI Table S6). The results revealed that this rotation requires overcoming an energy barrier, with the rotated geometry of **Cat 1** exhibiting significantly higher energy, exceeding 12.41 kcal mol⁻¹. This elevated energy demand suggests that such a structural transformation is thermodynamically favourable under the reaction conditions, which compensates for the energy requirement and enables the rotation. To elucidate the mechanism of CO₂ addition to epoxides catalyzed by **Cat 1b** (a rotational conformer of **Cat 1**), we performed DFT calculations

using the M06-2X/Def2-TZVPP level of theory. Fig. 8 presents the relative energy profile for the reaction of propylene oxide with CO₂, along with the structures of key intermediates.

Focusing on the mechanism of cyclic carbonate formation, the reaction is mainly divided into three steps. First, activation of the epoxide ring followed by the ring opening of the epoxide ring through iodide attack, second, activation of the CO₂ molecule by interaction with pyridine N and third, the insertion of CO₂ into epoxide and formation of the cyclic carbonate.¹⁰⁹ The mechanism and energy profile associated with this are presented in Fig. 8 and S39. The epoxide ring interacts with the phenolic –OH group, disrupting the N (imine)···HO (phenolic) hydrogen bond and forming a new O (epoxide)···HO (phenolic) bond, labeled as a. Propylene oxide coordinates with the highest-energy conformer **Cat 1b**, featuring an inter-molecular H-bond between the phenolic –OH and the propylene oxide O atom. The iodide anion opens the epoxide ring, forming an alkoxide intermediate c (+5.40 kcal mol⁻¹, endergonic). This occurs *via* transition state b with a barrier of 17.65 kcal mol⁻¹ relative to a. As mentioned in experimental studies (¹⁵N NMR), the CO₂ molecule is activated by the pyridine N atom.

Thus, the activation of CO₂ was further studied by showing the direct interaction of CO₂ with pyridine N. The literature reports that CO₂ interacts with pyridine nitrogen through van der Waals interactions, with a bond length of 2.77 Å.^{110–112} In the present case, this distance exceeds 2.89 Å, attributed to the influence of electronic repulsion of phenolic –OH groups. When CO₂ interacts with the nitrogen atom in pyridine, the CO₂ molecule, which is normally linear (with a bond angle of 180°), becomes slightly bent. This interaction causes the bond angle in the CO₂ molecule to decrease slightly, from 180° in its neutral

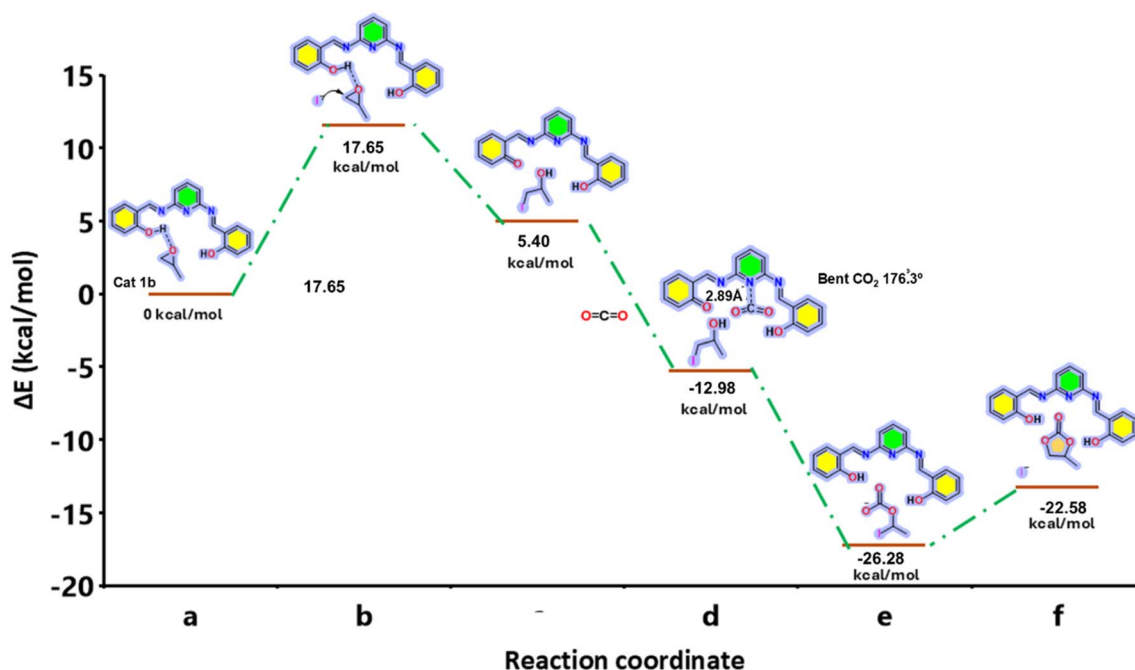


Fig. 8 The relative energy profile of ΔE (kcal mol⁻¹) of **Cat 1b** catalyzed addition of CO₂ to propylene oxide calculated at the M06-2X/Def2-TZVP level of theory.



state to approximately 176.3°. ¹¹² This bending indicates a subtle distortion in the geometry of CO₂ due to its interaction with pyridine nitrogen (optimized geometries are provided in the SI Fig. S36 and S39).

This exothermic reaction lowers the energy, forming intermediate d. CO₂ incorporation into intermediate d forms the hemicarbonate intermediate e in an exothermic reaction, with e having an energy of -26.28 kcal mol⁻¹. The ring-closure step is endothermic (+3.69 kcal mol⁻¹), positioning the product's energy at -22.58 kcal mol⁻¹ relative to the initial reactants a.

To further elucidate the role of the phenolic -OH group in the catalytic process, a deuterium exchange experiment was conducted on **Cat 1**. The ¹H NMR spectrum of the resulting deuterated catalyst exhibited a marked suppression of the -OH proton resonance, indicating its progressive conversion to the -OD form. Catalytic evaluations using the deuterated **Cat 1** under identical reaction conditions revealed a notable decrease in conversion (73%) relative to the non-deuterated **Cat 1**. ¹¹³⁻¹¹⁵ This diminished activity highlights the essential role of the -OH group in promoting epoxide activation, most likely *via* intramolecular hydrogen bonding with the imine moiety. These observations collectively underscore the functional significance of the phenolic -OH group in achieving high catalytic efficiency (Fig. S40 and S41) (Note in the SI, S42, S43 and S44).

To gain deeper structural insight into the proposed pyridine-CO₂ intermediate, we employed three spectrometric techniques *in situ* FT-IR, ¹³C NMR and HRMS under the standard reaction conditions. In the *in situ* FT-IR experiments, continuous introduction of CO₂ into a DMF solution of **Cat 1** led to the gradual emergence of a distinct absorption band at 1645 cm⁻¹. ¹¹⁶ This band is characteristic of the C=O stretching vibration of a carbamate species, consistent with CO₂ coordination at the pyridine N, and suggests suppression of other carbamate-containing species (Fig. S45). Complementary ¹³C NMR studies of **Cat 1**/styrene oxide/CO₂ mixtures revealed the emergence of a new resonance peak at 163.76 ppm, absent in spectra of **Cat 1** alone consistent with a carbamate carbon environment and corroborating formation of a pyridine-CO₂ adduct¹¹⁷ (Fig. S46a and b).

Further direct evidence was provided by ESI-HRMS, which revealed the formation of important intermediate species upon CO₂ introduction into the **Cat 1**/styrene oxide/TBAI reaction mixture (Fig. S47a-d). These intermediates reflect various binding modes of **Cat 1** with styrene oxide and/or CO₂. ¹¹⁸ Notably, the peak observed at *m/z* 438.1807 corresponds to the interaction of a single styrene oxide (S.O.) molecule with **Cat 1**. In contrast, the peak at *m/z* 557.2314 represents a complex wherein two S.O. molecules coordinate simultaneously with both hydroxyl (-OH) groups of **Cat 1**. Furthermore, the peak at *m/z* 624.2836, is attributed to the **Cat 1** complex coordinated to both styrene oxide and CO₂ as intermediate II (Fig. 9). The definitive identification of additional expected key intermediates, which are essential for elucidating the detailed mechanistic pathway of the **Cat 1**/styrene oxide/TBAI-catalyzed cycloaddition reaction, was also achieved through HRMS analysis. These findings are detailed in the SI (Fig. S48-S52).

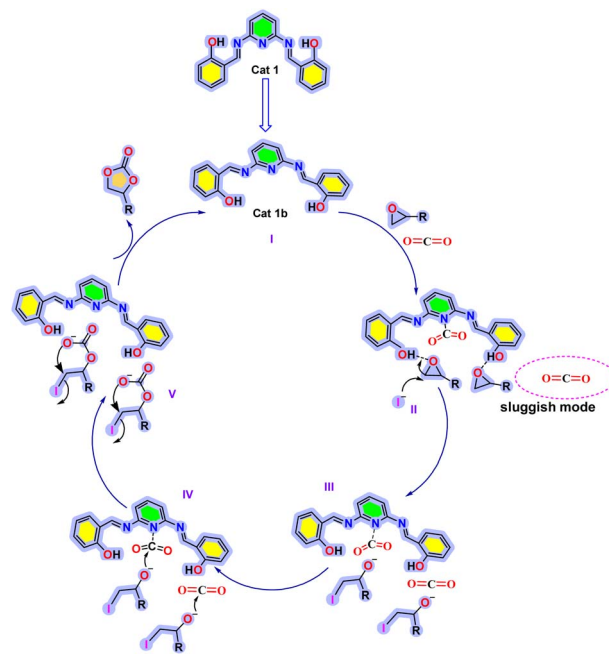


Fig. 9 Plausible catalytic cycle for **Cat 1**/TBAI-catalyzed addition of CO₂ to epoxides.

Finally, as shown in Fig. 9, we summarised the mechanism on the basis of our experimental results and previous mechanistic studies on related systems.^{67,91,119-123} The activation of the epoxide ring is initiated by a hydrogen-bond interaction between the hydrogen-bonded -OH group of **Cat 1b** (the most stable conformer, I) and the oxygen atom of the epoxide. This interaction significantly weakens the existing hydrogen bond between the -OH group and the imine nitrogen atom. Simultaneously, the iodide anion (I⁻) performs a nucleophilic attack on the less sterically hindered carbon atom of the epoxide ring, resulting in the formation of intermediate II. This step facilitates the ring opening of the epoxide, yielding the corresponding alkoxide intermediate III. Subsequently, CO₂ is activated through coordination with the N atom of the pyridine group, forming intermediate IV (Fig. S48-S52). Finally, nucleophilic addition of the alkoxide intermediate to the activated CO₂ generates an alkylcarbonate anion, denoted as intermediate V. This comprehensive mechanism underscores the interplay between catalytic activation, nucleophilic substitution, and CO₂ incorporation, validated through experimental and theoretical analyses. Finally, the catalytic cycle concludes with an intramolecular cyclization of the alkylcarbonate intermediate V, resulting in the formation of the cyclic carbonate product. This step also regenerates the catalyst, **Cat 1b**, and (TBAI), completing the catalytic process. Additionally, a non-hydrogen-bonded -OH group present in **Cat 1b** is also involved in the mechanism, albeit in sluggish mode.

Conclusions

In this study, we present a facile synthesis of non-toxic and inexpensive multifunctional binary organocatalytic systems



(Cat 1–5) for the synthesis of cyclic carbonates from epoxides and CO₂ under metal- and solvent-free conditions. These catalysts exhibit excellent performance in the conversion of both terminal and internal epoxides to cyclic carbonates, with the lowest catalyst and cocatalyst loadings, specifically by utilizing tetrabutylammonium iodide (TBAI) as a cocatalyst. Among the five systems, Cat 1 demonstrated the highest catalytic activity, attributed to its less sterically hindered structural configuration. Notably, thermal induction facilitated an *in situ* molecular flipping, altering the molecular planarity and orienting the active sites in close proximity, which is crucial for its enhanced catalytic efficiency. This conformational adjustment, coupled with DFT calculations and control experiments, confirmed the proposed geometry of Cat 1 and highlighted the role of the pyridine bridge in activating CO₂ during the reaction. Mechanistic investigations combining isotopic labeling and *in situ* IR, ¹³C NMR, and HRMS analyses provide robust insights into the cycloaddition pathway. Additionally, reusability tests and a scale-up experiment showcased the practicality of Cat 1, demonstrating that it can be recovered and reused up to six times without significant loss in catalytic activity. Furthermore, this study provides a foundation for future advancements in catalyst design by demonstrating how hydrogen bond manipulation and steric control can enhance catalytic efficiency. This approach could expand applications in CO₂ conversion technologies, from cyclic carbonates to broader polymeric materials, enabling sustainable solutions in carbon capture and utilization. Moving forward, incorporating computational modeling and exploring diverse functional groups may further optimize these catalysts, promoting scalable, low-energy processes for eco-friendly carbon utilization and other green chemical transformations. This study opens pathways for advanced catalyst design by optimizing hydrogen bond dynamics and steric configurations for greater efficiency. Future work can explore applications in broader CO₂ transformations, including polymer synthesis and sustainable carbon utilization.

Author contributions

V. Mishra and S. C. Peter conceived the idea and designed the research. V. Mishra and D. R. Deka planned and performed synthesis and catalysis experiments. S. Kediya conducted DFT calculations. D. Gaud aided in data analysis. D. R. Deka performed *in situ* IR measurements. S. Chakraborty carried out photoluminescence experiments. S. C. Peter and V. Mishra wrote the manuscript. All authors reviewed and contributed corrections to the final version.

Conflicts of interest

There are no conflicts to declare.

Data availability

The data supporting this article have been included as part of the supplementary information (SI). Supplementary information: detailed procedures for synthesis, catalysis, recyclability

studies, and experimental methodologies. It also contains characterization data including NMR, HRMS, photoluminescence (PL), UV-Vis spectroscopy, single-crystal X-ray diffraction (SCXRD), density functional theory (DFT) calculations, and supporting tables. See DOI: <https://doi.org/10.1039/d5sc02533h>.

Acknowledgements

Financial support from the Department of Science and Technology DST/TMDEWO/CCUS/CoE/2020/JNCASR(c) is gratefully acknowledged. SCP thanks DST for a Swarna Jayanti Fellowship (DST/SJF/GSA-02/2017–18) and VM thanks the University Grant Commission for a UGC-Kothari fellowship.

Notes and references

- 1 B. Ray, S. R. Churipard and S. C. Peter, *J. Mater. Chem. A*, 2021, **9**, 26498–26527.
- 2 A. Cherevotan, J. Raj and S. C. Peter, *J. Mater. Chem. A*, 2021, **9**, 27271–27303.
- 3 S. Roy, A. Cherevotan and S. Peter, *ACS Energy Lett.*, 2018, **3**, 1938–1966.
- 4 B. Schöffner, F. Schöffner, S. P. Verevkin and A. Börner, *Chem. Rev.*, 2010, **110**, 4554–4581.
- 5 S. Lawrenson, M. North, F. Peigneguy and A. Routledge, *Green Chem.*, 2017, **19**, 952–962.
- 6 M. Sathish, K.-J. Sreeram, J. Raghava Rao and B. Unni Nair, *ACS Sustainable Chem. Eng.*, 2016, **4**, 1032–1040.
- 7 D. J. Darensbourg, *Chem. Rev.*, 2007, **107**, 2388–2410.
- 8 X.-B. Lu and D. J. Darensbourg, *Chem. Soc. Rev.*, 2012, **41**, 1462–1484.
- 9 S. J. Poland and D. J. Darensbourg, *Green Chem.*, 2017, **19**, 4990–5011.
- 10 M. Bähr and R. Müllhaupt, *Green Chem.*, 2012, **14**, 483–489.
- 11 V. Laserna, G. Fiorani, C. J. Whiteoak, E. Martin, E. C. Escudero-Adán and A. W. Kleij, *Angew. Chem., Int. Ed.*, 2014, **53**, 10416–10419.
- 12 Y. J. Zhang, J. H. Yang, S. H. Kim and M. J. Krische, *J. Am. Chem. Soc.*, 2010, **132**, 4562–4563.
- 13 C.-C. Su, M. He, R. Amine, Z. H. Chen, R. Sahore, N. D. Rago and K. Amine, *Energy Storage Mater.*, 2019, **17**, 284–292.
- 14 C. Zhao, X. Luo, C. Chen and H. Wu, *Nanoscale*, 2016, **8**, 9511–9516.
- 15 M. Alves, B. Grignard, R. Mereau, C. Jerome, T. Tassaing and C. Detrembleur, *Catal. Sci. Technol.*, 2017, **7**, 2651–2684.
- 16 A. A. Chaugule, A. H. Tamboli and H. Kim, *Fuel*, 2017, **200**, 316–332.
- 17 Q. He, J. W. O'Brien, K. A. Kitselman, L. E. Tompkins, G. C. T. Curtis and F. M. Kerton, *Catal. Sci. Technol.*, 2014, **4**, 1513–1528.
- 18 B.-H. Xu, J.-Q. Wang, J. Sun, Y. Huang, J.-P. Zhang, X.-P. Zhang and S.-J. Zhang, *Green Chem.*, 2015, **17**, 108–122.
- 19 M. Cokoja, C. Bruckmeier, B. Rieger, W. A. Herrmann and F. E. Kühn, *Angew. Chem., Int. Ed.*, 2011, **50**, 8510–8537.



- 20 Z. Dai, Y. Tang, F. Zhang, Y. Xiong, S. Wang, Q. Sun, L. Wang, X. Meng, L. Zhao and F.-S. Xiao, *Chin. J. Catal.*, 2021, **42**, 618–626.
- 21 Q. Sun, Y. Jin, B. Aguila, X. Meng, S. Ma and F.-S. Xiao, *ChemSusChem*, 2017, **10**, 1160–1165.
- 22 L. Liu, S. Jayakumar, J. Chen, L. Tao, H. Li, Q. Yang and C. Li, *ACS Appl. Mater. Interfaces*, 2021, **13**, 29522–29531.
- 23 K. S. Song, P. W. Fritz and A. Coskun, *Chem. Soc. Rev.*, 2022, **51**, 9831–9852.
- 24 R. Luo, M. Chen, F. Zhou, J. Zhan, Q. Deng, Y. Yu, Y. Zhang, W. Xu and Y. Fang, *J. Mater. Chem.*, 2021, **9**, 25731–25749.
- 25 J. Liang, R.-P. Chen, X.-Y. Wang, T.-T. Liu, X.-S. Wang, Y.-B. Huang and R. Cao, *Chem. Sci.*, 2017, **8**, 1570–1575.
- 26 T. W. Li, F. Chen, M. Li and N. Liu, *Chin. J. Org. Chem.*, 2024, **44**, 3213–3222.
- 27 C. Martín, G. Fiorani and A. W. Kleij, *ACS Catal.*, 2015, **5**, 1353–1370.
- 28 A. Decortes, A. M. Castilla and A. W. Kleij, *Angew. Chem., Int. Ed.*, 2010, **49**, 9822–9837.
- 29 J. W. Comerford, I. D. V. Ingram, M. North and X. Wu, *Green Chem.*, 2015, **17**, 1966–1987.
- 30 R. Ma, L.-N. He and Y.-B. Zhou, *Green Chem.*, 2016, **18**, 226–231.
- 31 C. J. Whiteoak, E. Martin, M. M. Belmonte, J. Benet-Buchholz and A. W. Kleij, *Adv. Synth. Catal.*, 2012, **354**, 469–476.
- 32 J. A. Castro-Osma, K. J. Lamb and M. North, *ACS Catal.*, 2016, **6**, 5012–5025.
- 33 C. J. Whiteoak, N. Kielland, V. Laserna, E. C. Escudero-Adán, E. Martin and A. W. Kleij, *J. Am. Chem. Soc.*, 2013, **135**, 1228–1231.
- 34 G. Fiorani, W. Guo and A. W. Kleij, *Green Chem.*, 2015, **17**, 1375–1389.
- 35 M. Cokoja, M. E. Wilhelm, M. H. Anthofer, W. A. Herrmann and F. E. Kühn, *ChemSusChem*, 2015, **8**, 2436–2454.
- 36 M. Alves, B. Grignard, R. Mereau, C. Jerome, T. Tassaing and C. Detrembleur, *Catal. Sci. Technol.*, 2017, **7**, 2651–2684.
- 37 L. Guo, K. J. Lamb and M. North, *Green Chem.*, 2021, **23**, 77–118.
- 38 Y.-B. Wang, D.-S. Sun, H. Zhou, W.-Z. Zhang and X.-B. Lu, *Green Chem.*, 2015, **17**, 4009–4015.
- 39 B. Chen, J. Zeng, S. Zhang and Y. Zhang, *Chem. Sci.*, 2024, **15**, 14851–14864.
- 40 B. Wang, Z. Luo, E. H. M. Elageed, S. Wu, Y. Zhang, X. Wu, F. Xia, G. Zhang and G. Gao, *ChemCatChem*, 2016, **8**, 830–838.
- 41 Z. Zhang, F. Fan, H. Xing, Q. Yang, Z. Bao and Q. Ren, *ACS Sustainable Chem. Eng.*, 2017, **5**, 2841–2846.
- 42 Z. Guo, Y. Hu, S. Dong, L. Chen, L. Ma, Y. Zhou, L. Wang and J. Wang, *Chem Catal.*, 2022, **2**, 519–530.
- 43 X. Wang, Y. Zhou, Z. Guo, G. Chen, J. Li, Y. Shi, Y. Liu and J. Wang, *Chem. Sci.*, 2015, **6**, 6916–6924.
- 44 P. Sudarsanam, R. Zhong, S. Van den Bosch, S. M. Coman, V. I. Parvulescu and B. F. Sels, *Chem. Soc. Rev.*, 2018, **47**, 8349–8402.
- 45 A. Rostami, M. Mahmoodabadi, A. Hossein Ebrahimi, H. Khosravi and A. Al-Harrasi, *ChemSusChem*, 2018, **11**, 4262–4268.
- 46 H. Büttner, J. Steinbauer and T. Werner, *ChemSusChem*, 2015, **8**, 2655–2669.
- 47 R. R. Kuruppathparambil, T. Jose, R. Babu, G.-Y. Hwang, A. C. Kathalikkattil, D.-W. Kim and D.-W. Park, *Appl. Catal., B*, 2016, **182**, 562–569.
- 48 J. Li, D. Jia, Z. Guo, Y. Liu, Y. Lyu, Y. Zhou and J. Wang, *Green Chem.*, 2017, **19**, 2675–2686.
- 49 C. Calabrese, L. F. Liotta, E. Carbonell, F. Giacalone, M. Gruttadauria and C. Aprile, *ChemSusChem*, 2017, **10**, 1202–1209.
- 50 S. Duan, X. Jing, D. Li and H. Jing, *J. Mol. Catal. A: Chem.*, 2016, **411**, 34–39.
- 51 J. Tharun, K.-M. Bhin, R. Roshan, D. W. Kim, A. C. Kathalikkattil, R. Babu, H. Y. Ahn, Y. S. Won and D.-W. Park, *Green Chem.*, 2016, **18**, 2479–2487.
- 52 Z. Zhang, F. Fan, H. Xing, Q. Yang, Z. Bao and Q. Ren, *ACS Sustainable Chem. Eng.*, 2017, **5**, 2841–2846.
- 53 T. Jose, S. Cañellas, M. A. Pericàs and A. W. Kleij, *Green Chem.*, 2017, **19**, 5488–5493.
- 54 T. Wang, D. Zheng, J. Zhang, B. Fan, Y. Ma, T. Ren, L. Wang and J. Zhang, *ACS Sustainable Chem. Eng.*, 2018, **6**, 2574–2582.
- 55 H. Büttner, J. Steinbauer and T. Werner, *ChemSusChem*, 2015, **8**, 2655–2669.
- 56 Y. Toda, Y. Komiyama, A. Kikuchi and H. Suga, *ACS Catal.*, 2016, **6**, 6906–6910.
- 57 Y. Wu, Y. Zhao, R. Li, B. Yu, Y. Chen, X. Liu, C. Wu, X. Luo and Z. Liu, *ACS Catal.*, 2017, **7**, 6251–6255.
- 58 W. Wang, Y. Wang, C. Li, L. Yan, M. Jiang and Y. Ding, *ACS Sustainable Chem. Eng.*, 2017, **5**, 4523–4528.
- 59 Z. Xu, M. Wang and M. P. Shaver, *Chem. Sci.*, 2024, **15**, 15745–15750.
- 60 A. Duval and L. Avérous, *ACS Sustainable Chem. Eng.*, 2017, **5**, 7334–7343.
- 61 L. Martínez-Rodríguez, J. Otalora Garmilla and A. W. Kleij, *ChemSusChem*, 2016, **9**, 749–755.
- 62 Y. Zhi, P. Shao, X. Feng, H. Xia, Y. Zhang, Z. Shi, Y. Mu and X. Liu, *J. Mater. Chem. A*, 2018, **6**, 374–382.
- 63 Y. A. Rulev, Z. T. Gugkaeva, A. V. Lokutova, V. I. Maleev, A. S. Peregodov, X. Wu, M. North and Y. N. Belokon, *ChemSusChem*, 2017, **10**, 1152–1159.
- 64 S. Arayachukiat, C. Kongtes, A. Barthel, S. V. C. Vummaleti, A. Poater, S. Wannakao, L. Cavallo and V. D'Elia, *ACS Sustainable Chem. Eng.*, 2017, **5**, 6392–6397.
- 65 S. Kaneko and S. Shirakawa, *ACS Sustainable Chem. Eng.*, 2017, **5**, 2836–2840.
- 66 S. Sopena, E. Martin, E. C. Escudero-Adán and A. W. Kleij, *ACS Catal.*, 2017, **7**, 3532–3539.
- 67 N. Liu, Y.-F. Xie, C. Wang, S.-J. Li, D. Wei, M. Li and B. Dai, *ACS Catal.*, 2018, **8**, 9945–9957.
- 68 A. Rostami, A. Ebrahimi, M. Al-Jassasi, S. Mirzaei and A. Al-Harrasi, *Green Chem.*, 2022, **24**, 9069–9083.
- 69 S. Sopena, G. Fiorani, C. Martín and A. W. Kleij, *ChemSusChem*, 2015, **8**, 3248–3254.



- 70 C. J. Whiteoak, A. H. Henseler, C. Ayats, A. W. Kleij and M. A. Pericàs, *Green Chem.*, 2014, **16**, 1552–1559.
- 71 C. J. Whiteoak, A. Nova, F. Maseras and A. W. Kleij, *ChemSusChem*, 2012, **5**, 2032–2038.
- 72 F. Della Monica, A. Buonerba, A. Grassi, C. Capacchione and S. Milione, *ChemSusChem*, 2016, **9**, 3457–3464.
- 73 A. M. Hardman-Baldwin and A. E. Mattson, *ChemSusChem*, 2014, **7**, 3275–3278.
- 74 M. E. Wilhelm, M. H. Anthofer, M. Cokoja, I. I. E. Markovits, W. A. Herrmann and F. E. Kühn, *ChemSusChem*, 2014, **7**, 1357–1360.
- 75 S. Gennen, M. Alves, R. Méreau, T. Tassaing, B. Gilbert, C. Detrembleur, C. Jerome and B. Grignard, *ChemSusChem*, 2015, **8**, 1845–1849.
- 76 J. Wang and Y. Zhang, *ACS Catal.*, 2016, **6**, 4871–4876.
- 77 V. B. Saptal and B. M. Bhanage, *ChemSusChem*, 2017, **10**, 1145–1151.
- 78 S. Sopeña, E. Martin, E. C. Escudero-A and A. W. Kleij, *ACS Catal.*, 2017, **7**, 3532–3539.
- 79 U. Fegade, S. Attarde and A. Kuwar, *Chem. Phys. Lett.*, 2013, **584**, 165–171.
- 80 C. Garcias-Morales, J. E. Maldonado, A. A. Castolo, C. M. P. Berumen, M. A. Lobato, M. A. Rodriguez and A. E. Roa, *J. Mol. Struct.*, 2021, **1228**, 129444.
- 81 M. D. Milošević, A. D. Marinković, P. Petrović, A. Klaus, M. G. Nikolić, N. Ž. Prlainović and I. N. Cvijetić, *Bioorg. Chem.*, 2020, **102**, 104073.
- 82 N. Karaboecek, S. Karaboecek and F. Kormali, *Turk. J. Chem.*, 2007, **31**, 271–277.
- 83 A. H. Kianfar, M. K. Boudani, M. Roushani and M. Shamsipur, *J. Iran. Chem. Soc.*, 2012, **9**, 449–453.
- 84 A. G. Ivanov, B. V. Chernitsa, V. V. Shamanin and L. V. Vinogradova, *Russ. J. Appl. Chem.*, 2014, **87**, 1693–1699.
- 85 F. Shabani, K. Mehrani, S. Ghammamy, M. R. Rezakhani, S. A. S. Sadjadi, R. Rahimi, S. Asili and A. Hematimoghadam, *Asian J. Chem.*, 2009, **21**, 6587.
- 86 M. Salavati-Niasari and M. Shaterian, *J. Porous Mater.*, 2008, **15**, 581–588.
- 87 N. Galić, D. Matković-Čalogović and Z. Cimerman, *J. Mol. Struct.*, 1997, **406**, 153–158.
- 88 X. Wu, C. Chen, Z. Guo, M. North and A. Whitwood, *ACS Catal.*, 2019, **9**, 1895–1906.
- 89 N. Galić, D. Matković-Čalogović and Z. Cimerman, *J. Mol. Struct.*, 1997, **406**, 153–158.
- 90 S. Subramanian, J. Park, J. Byun, Y. Jung and C. T. Yavuz, *ACS Appl. Mater. Interfaces*, 2018, **10**, 9478–9484.
- 91 C. J. Whiteoak, A. Nova, F. Maseras and A. W. Kleij, *ChemSusChem*, 2012, **5**, 2032–2038.
- 92 X. Wu, C. Chen, Z. Guo, M. North and A. C. Whitwood, *ACS Catal.*, 2019, **9**, 1895–1906.
- 93 L. Wang, G. Zhang, K. Kodama and T. Hirose, *Green Chem.*, 2016, **18**, 1229–1233.
- 94 R. Azzouz, V. C. Moreno, C. Herasme-Grullon, V. Levacher, L. Estel, A. Ledoux, S. Derrouiche, F. Marsais and L. Bischoff, *Synlett*, 2020, **31**, 183–188.
- 95 M. Liu, X. Wang, Y. Jiang, J. Sun and M. Arai, *Catal. Rev.*, 2019, **61**, 214–269.
- 96 C. M. Thomas and B. Bibal, *Green Chem.*, 2014, **16**, 1687–1699.
- 97 A. Dalla Cort, F. Gasparrini, L. Lunazzi, L. Mandolini, A. Mazzanti, C. Pasquini, M. Pierini, R. Rompietti and L. Schiaffino, *J. Org. Chem.*, 2005, **70**, 8877–8883.
- 98 S. Liang, H. Liu, T. Jiang, J. Song, G. Yang and B. Han, *Chem. Commun.*, 2011, **47**, 2131–2133.
- 99 A. M. Hardman-B and A. E. Mattson, *ChemSusChem*, 2014, **7**, 3275–3278.
- 100 H. A. Mohammed and N. I. Taha, *Int. J. Org. Chem.*, 2017, **7**, 412–419.
- 101 R. Marek, A. Lycka, E. Kolehmainen, E. Sievanen and J. Tousek, *Curr. Org. Chem.*, 2007, **11**, 1154–1205.
- 102 R. Chen, Q. Li, Z. Zhang, K. Xu, L. Sun, J. Ma, T. Wang, X. Mu, Y. Xi and L. C. Cao, *J. Photochem. Photobiol. A*, 2023, **436**, 114335.
- 103 Ö. Güngör, *Inorg. Chim. Acta*, 2025, **574**, 122410.
- 104 M. Umare, D. A. Patel, V. Bhardwaj, A. K. Sk and S. K. Sahoo, *J. Fluoresc.*, 2023, **33**, 601–611.
- 105 Z. Wu, J. Xu, Z. Wu, R. Zhao and L. Hou, *J. Photochem. Photobiol. A*, 2024, **453**, 115668.
- 106 K. Ponnusamy, K. Ramamurthy and S. Chellappan, *J. Phys. Chem. A*, 2020, **124**, 1885–1895.
- 107 L. Guo, K. J. Lamb and M. North, *Green Chem.*, 2021, **23**, 77–118.
- 108 J. Chen, G. Chiarioni, G.-J. W. Euverink and P. P. J. Pescarmona, *Green Chem.*, 2023, **25**, 9744–9759.
- 109 V. Mishra and S. C. Peter, *Chem Catal.*, 2024, **4**, 100796.
- 110 K. D. Vogiatzis, A. Mavrandonakis, W. Klopffer and G. E. Froudakis, *ChemPhysChem*, 2009, **10**, 374–383.
- 111 J. L. Doran, B. Hon and K. R. Leopold, *J. Mol. Struct.*, 2012, **1019**, 191–195.
- 112 P. Wang, Q. Lv, Y. Tao, L. Cheng, R. P. Li, Y. Jiao, C. Fang, H. Li, C. Geng, C. Sun, J. Ding, H. Wan and G. Guan, *Mol. Catal.*, 2023, **544**, 113157.
- 113 P. E. Hansen, *Molecules*, 2022, **27**, 2405.
- 114 V. V. Mulloyarova, D. O. Ustimchuk, A. Filarowski and P. M. Tolstoy, *Molecules*, 2020, **25**, 1907.
- 115 D. F and M. V. Gemmeren, *J. Chem. Educ.*, 2024, **101**, 3410–3417.
- 116 Y.-B. Zhou, F. Chen, Z.-H. Du, B.-Y. Liu and N. Liu, *Inorg. Chem.*, 2024, **63**, 16491–16506.
- 117 Y. Luo, F. Chen, H. Zhang, J. Liu and N. Liu, *J. Org. Chem.*, 2023, **88**, 15717–15725.
- 118 Y.-H. Luo, S. Tao, F. Chen, Z.-H. Du, H. Zhang, M. Li and N. Liu, *Catal. Sci. Technol.*, 2024, **14**, 6692–6700.
- 119 J. Ma, J. Liu, Z. Zhang and B. Han, *Green Chem.*, 2012, **14**, 2410–2420.
- 120 L. Wang, G. Zhang, K. Kodama and T. Hirose, *Green Chem.*, 2016, **18**, 1229–1233.
- 121 T. Werner and H. C. Büttner, *ChemSusChem*, 2014, **7**, 3268–3271.
- 122 B. Wang, L. Wang, J. Lin, C. Xia and W. Sun, *ACS Catal.*, 2023, **13**, 10386–10393.
- 123 W.-W. Yu, X.-G. Meng, Z.-Y. Gan, W. Li, Y.-L. Zhang and J. Zhou, *Catal. Sci. Technol.*, 2024, **14**, 6215–6223.

